Electronic Supplementary Material (ESI) for Energy & Environmental Science

Supporting Information

Revealing the Atomic Structure and Strontium Distribution in Nanometer-Thick $La_{0.8}Sr_{0.2}CoO_{3-\delta}$ Grown on (001)-Oriented $SrTiO_3$

Zhenxing Feng[1, 2], Yizhak Yacoby[4], Wesley T. Hong[1, 3], Hua Zhou[5], Michael D. Biegalski[6], Hans M. Christen[6], and Yang Shao-Horn[1, 2, 3, *]

[1]*Electrochemical Energy Laboratory,* [2]*Department of Mechanical Engineering,* [3]*Department of Materials Science and Engineering, Massachusetts Institute of Technology, Cambridge, Massachusetts, 02139, USA*

[4]*Racah Institute of Physics, Hebrew University, Jerusalem, 91904, Israel*

[5]*Advanced Photon Source, Argonne National Laboratory, Argonne, Illinois, 60439, USA*

[6]*Center for Nanophase Materials Science, Oak Ridge National Laboratory, Oak Ridge, Tennessee, 37831, USA*

[*]Corresponding author (e-mail: shaohorn@mit.edu)

Index **Page**

Supplementary Methods

Pulsed Laser Deposition (PLD) Target Synthesis and Growth.

$La_{0.8}Sr_{0.2}CoO_{3-\delta}$ (LSCO) powders were synthesized by a solid-state reaction using a stoichiometric mixture of La_2O_3, $SrCO_3$, and Co_3O_4 (Alfa Aesar, USA) 1,000°C in air for 12 hours.

Polished $SrTiO_3$(001) (STO, 10 × 10 × 1 mm^3, CrysTec) single crystal substrates were acid-etched in HF buffered solution for 30 s and subsequently annealed in oxygen at 1050 °C for 2 hours to obtain atomically flat surfaces. Epitaxial thin films of LSCO on STO were prepared by pulsed laser deposition (PLD) at 557 °C under 50 mTorr O_2. PLD was done under the following conditions: KrF excimer laser (λ = 248 nm), 10 Hz pulse rate, ~50 mJ pulse energy, and the growth rate ~ 70 pulses per LSCO unit cell.

Coherent Bragg Rod (COBRA) Measurements, Analysis and Error Analysis.

COBRA analysis[1] starts with building an initial structure model, which is the bulk STO substrate with a pseudomorphic LSCO film (Table S1). The top four unit cells of the substrate and the film structures were allowed to deform. The complex scattering factors (CSFs) of the initial model, $\mathbf{S_0}$, can be calculated and compared with the measured diffraction intensities, $|\mathbf{T}|^2$. The difference comes from the CSFs of an unknown part, $\mathbf{U_0}$:

$$\left|\mathbf{S_0}+\mathbf{U_0}\right|^2=\left|\mathbf{T}\right|^2. \quad \text{Eq. (S1)}$$

The CSFs vary continuously along the Bragg rods. By assuming that the CSFs of the unknown part vary slowly compared to $\mathbf{S_0}$ and $\mathbf{T}$, the amplitude and phase of $\mathbf{U_0}$ can be solved within adjacent points along the Bragg rod, and then added to initial $\mathbf{S_0}$ to obtain $\mathbf{S_{10}}$**.** This CSF is converted to real space and confining its values to be positive within the sample and zero out side it we obtain a new reference EDY. We now calculate the new CSF, S_1 and proceed as before until $|S_n|^2$ is aproximately |equal to $|T|^2$..Using COBRA and the difference map method[2], very good agreement was achieved between the experimental and the diffraction intensities calculated using the COBRA determined EDY for all Bragg rods in our case with an overall X-

ray reliability factor $R = \frac{\sum \left| |F_o| - |F_c| \right|}{\sum |F_0|} < 0.02$, where $|F_0|$ and $|F_c|$ are the observed and the calculated diffraction amplitude, respectively.

By analyzing the 3D EDY one can obtain important information of the system, such as atomic positions and occupations of elements. The error bars of the parameters of interest, such as the apical oxygen positions in this work, have been estimated for each individual sample using the following method, referred as Noise Analysis. This method resembles the widely used Bootstrap resampling approach for uncertainty estimations in statistical analysis.[3]

Differential COBRA[4] uses the energy-dependence of the elemental scattering cross-sections. At each point along the rods the difference between the diffraction intensities is measured just below and just above the absorption edge of the element of interest. The main sources of error in measuring the diffraction intensities are systematic, coming from uncertainties in the background subtraction and from errors in determining the position along the Bragg rod and the diffraction phases: the advantage of the differential method is to significantly reduce the systematic errors, thus increasing the accuracy of the measured difference. If the entire data set is measured and analyzed at one energy at a time, these errors are largely independent and propagate, resulting in increased uncertainty[5]. On the other hand, if the diffraction intensity is measured differentially, i.e. if one measures the difference in the diffraction intensities at the two energies at each point along the Bragg rod, the errors are partially canceled and the uncertainty is decreased.

Although the change in the scattering cross-section across the absorption edge is smaller than the change that can be obtained at energies just below and far below the absorption edge it is advantageous to use the first energy pair rather than the second. The reason is that in the first case the difference between the two energies is very small (~20 eV). This allows us to use high-resolution piezo actuators to adjust the sample orientation such that the diffraction intensities are measured at both energies at exactly the same point along the Bragg rod.

To analyze the data and determine the concentration of a chosen atomic species, it is necessary to know its cross section at the two energies used. At energies close to the absorption edge, the complex scattering cross section depends on the environment of the probe atom and needs to be determined experimentally. This was performed by measuring the X-ray

fluorescence as a function of incident beam photon energy and by using the calculated complex scattering cross-section far away from the edge and the Kramers-Kronig relationship[4].

Using COBRA along with the difference map, the effective EDY, $\rho_L = \rho(x, y, z)$, can be determined from the full data set measured at the lower energy. The EDY can then be used to calculate the diffraction intensity $I_L(h, k, l)$ along the different rods. At the higher energy, due to the change in the complex scattering factor, the effective EDY will change to

$$\rho_H = \rho_L + \sum_i \rho_i^A(x_i, y_i, z_i) c_i^A \Delta f_A, \qquad \text{Eq. (S2)}$$

$$\text{where} \quad \hat{\rho}_i^A = \frac{\hat{\rho}_i}{f_A^r + f_o \Phi(\vec{k})},$$

$\hat{\rho}_i$ is the Fourier transform of the electron density ρ_i around site i, f_A^r, f_o are the real part of the anomalous and the ordinary scattering cross-sections at the low energy, respectively, and $\Phi(\vec{k})$ is the three dimensional atomic form factor of Sr normalized to unity at $k = 0$; c_i^A is the fraction of the electrons close to site i that belong to Sr and Δf_A is the difference between the complex anomalous scattering factors of Sr at the higher and lower energies.. The change in the EDY, $\Delta\rho$, results in a change in the diffraction intensities, $I_H(h, k, l) = I_L(h, k, l) + \Delta I$. Therefore, by refining the c_i^A parameters, ΔI can be fitted to the measured differential signal, which allows us to determine the individual occupancies of the probe atom within the folded unit cell.

In fitting the differential COBRA data, the Sr concentration (or occupation of Sr in A site of ABO_3 perovskite) in each La/Sr layer, including the top six Sr layers of the substrate, were set initially to the nominal composition but left open for fitting to the six differential Bragg rods simultaneously. Since layers are not fully occupied in the particle region due to the much lower La/Sr EDY peaks, and Sr concentration represents the Sr/(Sr+La) ratio in the occupied portion only. In our case, we have 19 parameters for fitting but more than 125 independent data points from the differential measurements. Therefore the results from the differential COBRA analysis are reliable and robust.

Surface Coverage Measurements from AFM and COBRA.

The particle surface coverage of LSCO has been calculated by adding up the areas of particles at certain heights from AFM data. The background of the terraces from STO substrate was subtracted before particle coverage estimation. A continuous curve can be drawn as shown in Figure S1b. Similarly the surface coverage can be calculated from COBRA data. The area coverage of atomic planes at different heights has been analyzed by integrating the EDY in 3D around a given plane and comparing it to the expected integrated EDY of a fully covered plane, e.g. the integrated EDY of Co in a plane in the particle region was normalized to the integrated EDY of Co in a fully covered plane. The coverage of atomic planes at different Z positions (particle heights) is also shown in Figure 1Sb and is reasonably consistent with that calculated from AFM images.

In-Plane Lattice Constants Determination.

To estimate the in-plane lattice constants, several 2D in-plane cuts were performed to determine the La/Sr in-plane peak broadening relative to the substrate Sr peaks. The ratio of film La/Sr in-plane peak $FWHM_f$ with respect to substrate Sr $FWHM_{sub}$ (Figure S9). This in-plane peak broadening is proportional to the difference between in-plane lattice constants of the film and the substrate, and due to the folding, it is also proportional to the average number of unit cells between dislocations. Here, we assume that the distance between dislocations in the LSCO film is about equal to the surface particle diameter. The diameter of the islands is about $N = 25$ unit cells (determined from AFM images). Therefore, the in-plane LSCO lattice constants can be calculated using the following equation,

$$|a_{STO} - a_{LSC}| N = FWHM_f - FWHM_{sub}. \qquad \text{Eq. (S4)}$$

The average in-plane peak broadening is found to be 0.03 nm, resulting in an average unit cell close to that of STO (~ 3.89-3.90 Å). Thus the in-plane unit cell size is very close to the in-plane lattice size of the substrate, indicating a very good in-plane registry.

Calculation of the Oxygen Octahedral Distortion in Perovskite ABO_3 Oxides.

In ABO_3 structure, atom B is located at the unit cell center (0.5 0.5 0.5) and is surrounded by 6 oxygen atoms at (0.5 0.5 0) and symmetry equivalent positions to form a corner-sharing BO_6 octahedra, as seen from Figure 3 inset. The octahedral tilts in the perovskite-type

unit cell can be described as a combination of rotations about three symmetry axes of the pseudocubic unit cell: $[100]_c$, $[010]_c$, and $[001]_c$.[6] According to Glazer[7], the relationship between the tilt angle and pseudocubic axial lengths can be described as follows:

$$a_p = \xi \cos\beta \cos\gamma$$
$$b_p = \xi \cos\alpha \cos\gamma$$
$$c_p = \xi \cos\alpha \cos\beta, \qquad \text{Eq. (S3)}$$

where ξ is the the anion-anion distance through the center of the octahedron.

For bulk LSCO, the O-Co-O distance can be calculated to be 3.85 Å and the pseudocubic unit cell size is $a_p=b_p=c_p=3.803$ Å[8]. Therefore using Eq. S3, the octahedral tilt is $\alpha=\beta=\gamma=6.3^o$.

Table S1: Atomic positions of each elements of the initial model, which is used for COBRA analysis.

	x	*y*	*z*
Film (10 unit cells) a_{LSCO}=b_{LSCO} = 3.905 Å c_{LSCO} = 3.75 Å			
Co	0.5	0.5	0
O	0	0.5	0
O	0.5	0	0
La/Sr	0	0	-0.5
O	0.5	0.5	-0.5
Substrate (6 unit cells) a_{STO} =3.905 Å			
Ti	0.5	0.5	0
O	0	0.5	0
O	0.5	0	0
Sr	0	0	-0.5
O	0.5	0.5	-0.5

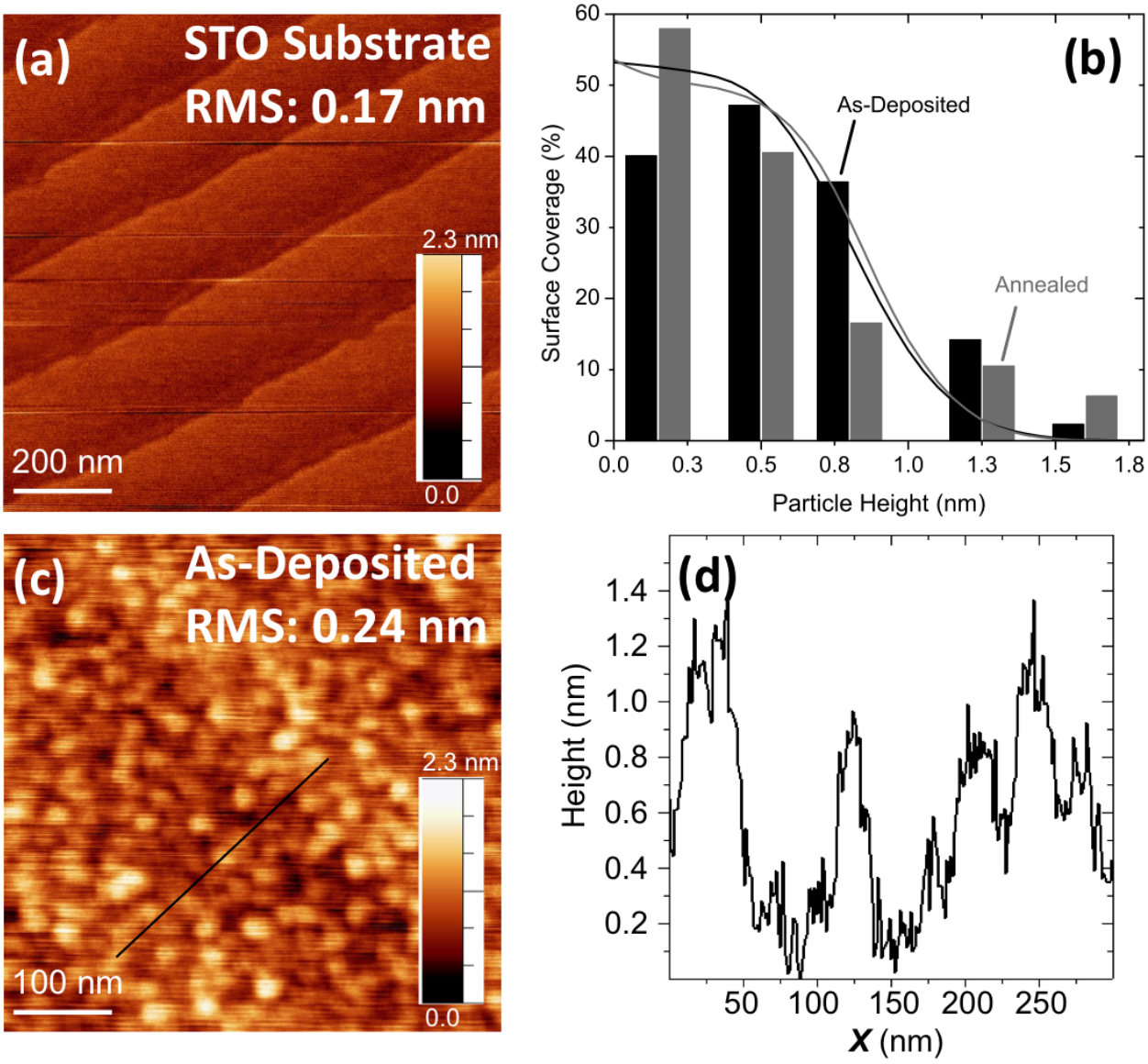

Figure S1. (a) 1 × 1 μm^2 AFM image of blank $SrTiO_3$ substrate with clear terraces separate by ~ 4 Å. (b) The particle surface coverage at different heights calculated from AFM data (lines) from Figure 1 and COBRA results (bars) for as-deposited and annealed from Figure 3 by integrating electron density at corresponding heights. (c) High resolution atomic-force microscopy (0.5 × 0.5 μm^2) with small particles on terraces, indicating the Stranski-Krastanov mode or mixed layer-by-layer/island growth. (d) Height profile of the dark line in (c) shows these particles are ~10 nm in diameter and ~1-2 nm in height.

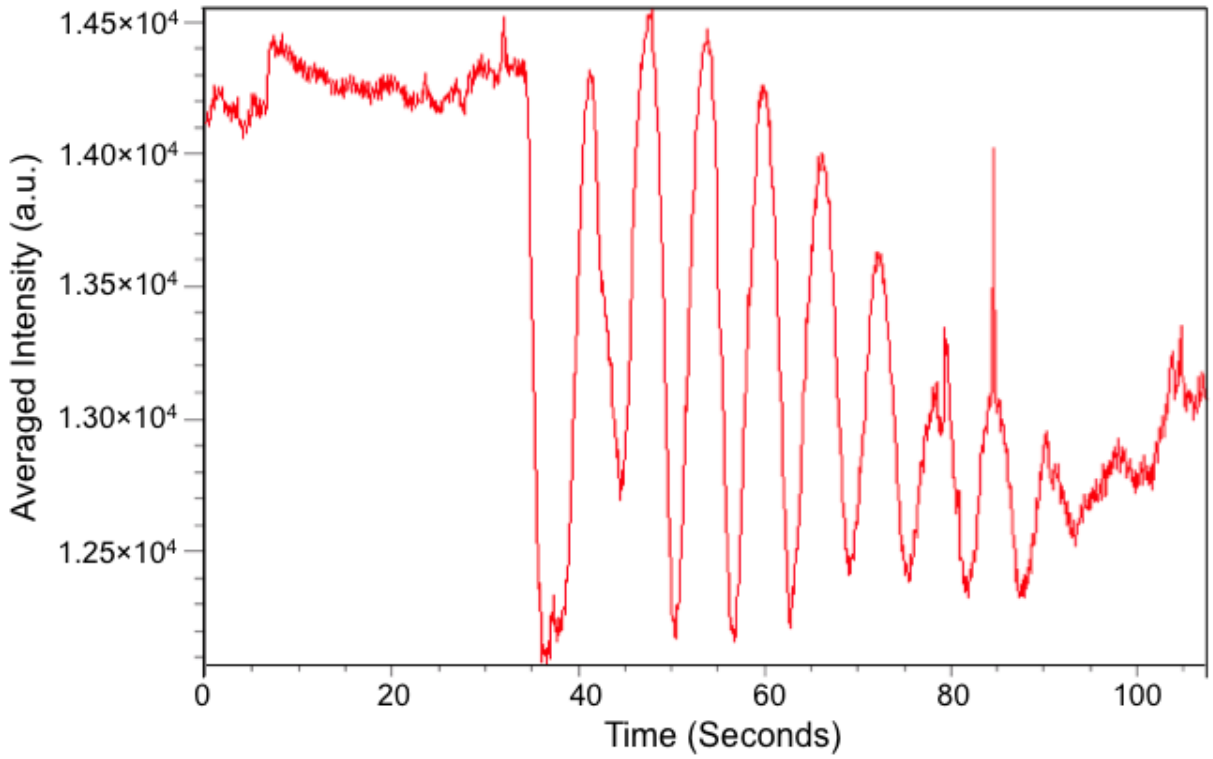

Figure S2. RHEED oscillations (intensity of the specular reflection measured as a function time) recorded during growth of LSCO/STO. These oscillations indicate the initial layer-by-layer growth and then mixed islands and layer-by-layer growth mode.

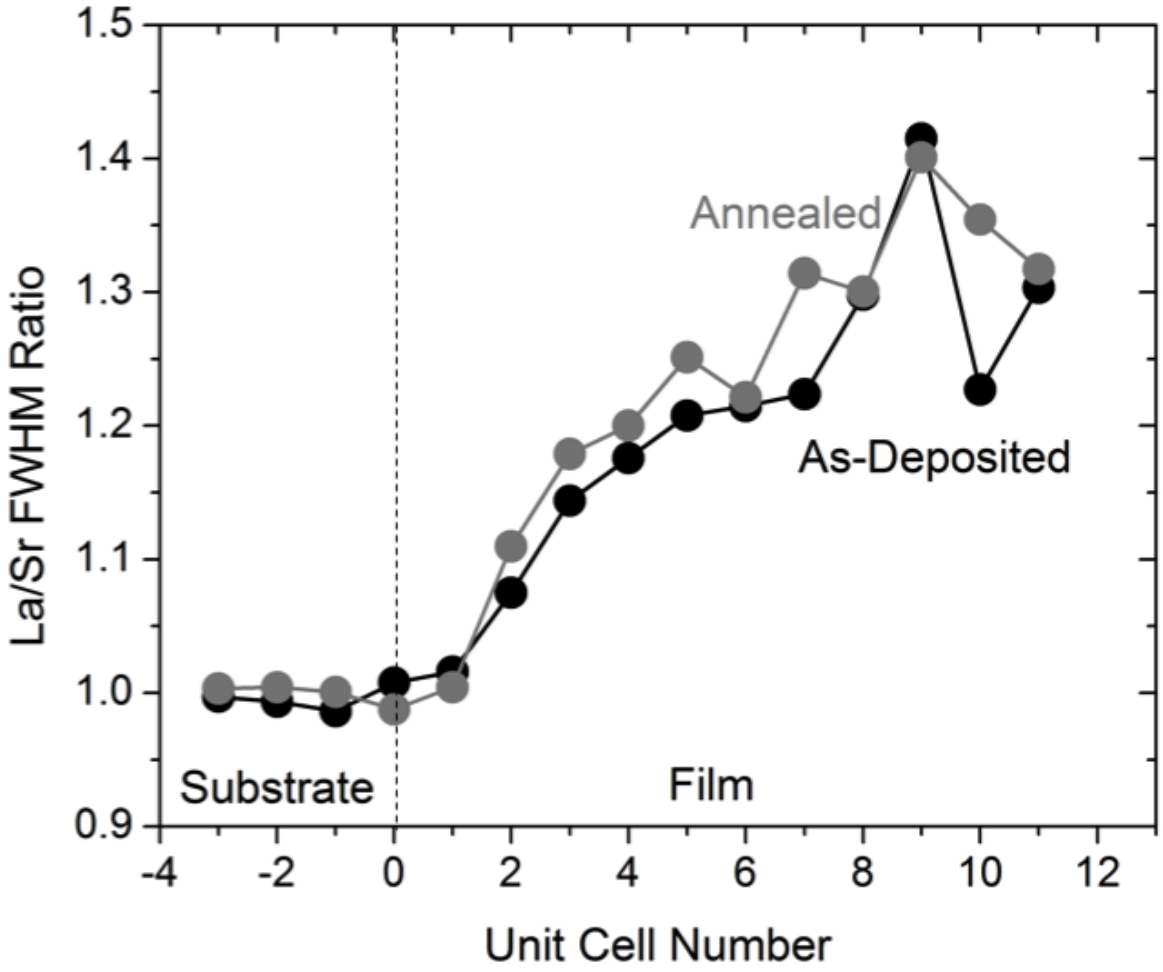

Figure S3. Layer-by-layer in-plane La/Sr FWHM normalized to the substrate Sr FWHM taken as unity. The dashed line represents the nominal substrate/film interface.

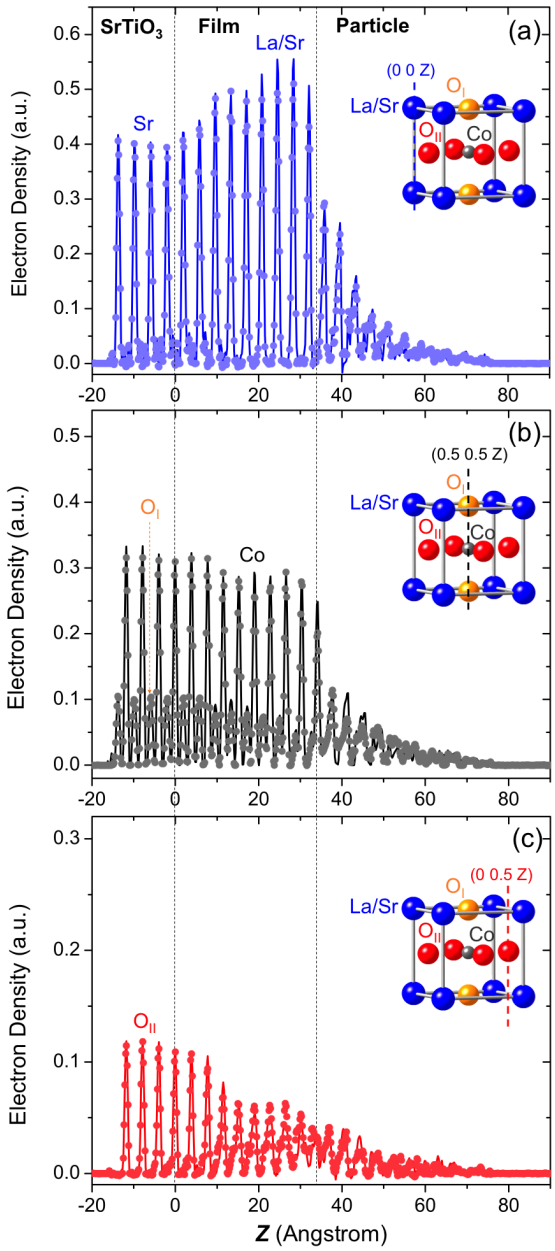

Figure S4. The electron density (EDY) of as deposited (color lines) and annealed (light dots) systems along three lines shown in the crystal model insets. (a) The EDY along the (0 0 Z) line through La/Sr atoms, (b) the EDY along the (0.5 0.5 Z) line through Co, Ti, and O_I atoms, (c) the EDY along the (0 0.5 Z) line through O_{II} atoms for as-deposited (dark color) and annealed (grey/light color) samples. The topmost six unit cells of the substrate are included in the structure determination. The dashed line represents the nominal substrate/film interface and "bulk" film/particle interface.

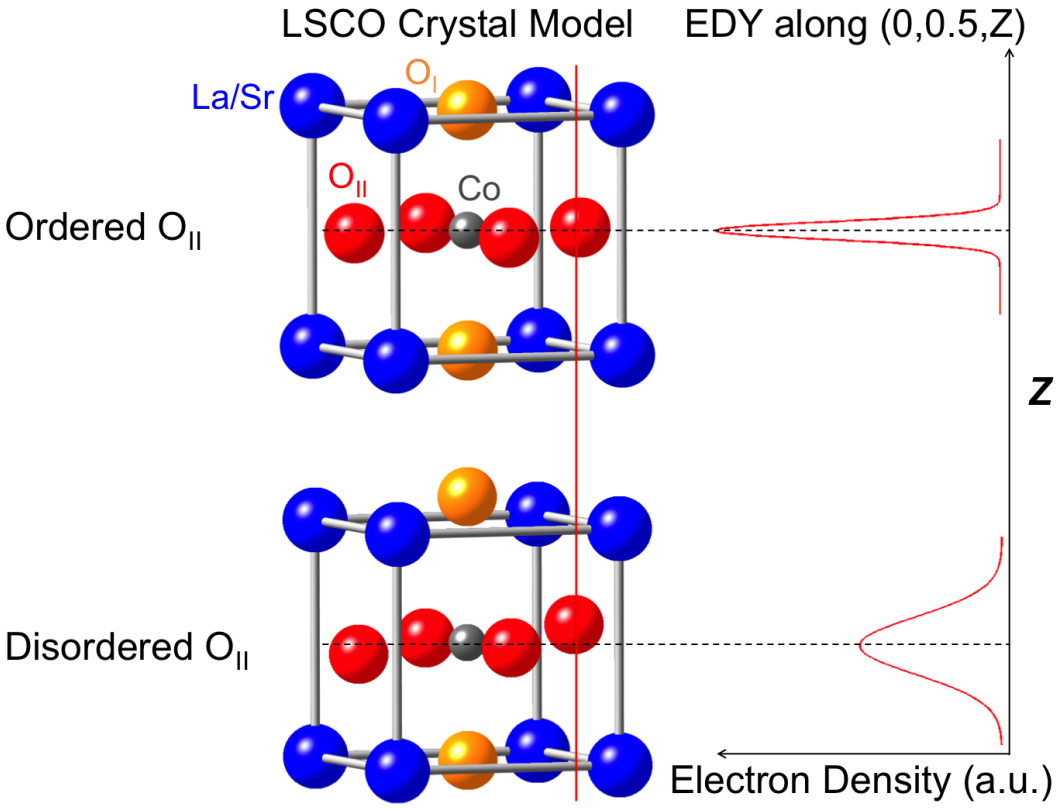

Figure S5. Schematic models show the ordered and disordered atoms (O_{II} in this case) and their EDY along (0 0.5 Z) line, respectively. Ordered O_{II} occupy centrosymmetric crystallographic positions and the EDY peak is sharp, while deviation of O_{II} from centrosymmetric crystallographic positions results in the broader and decreased EDY peak in the folded structure.

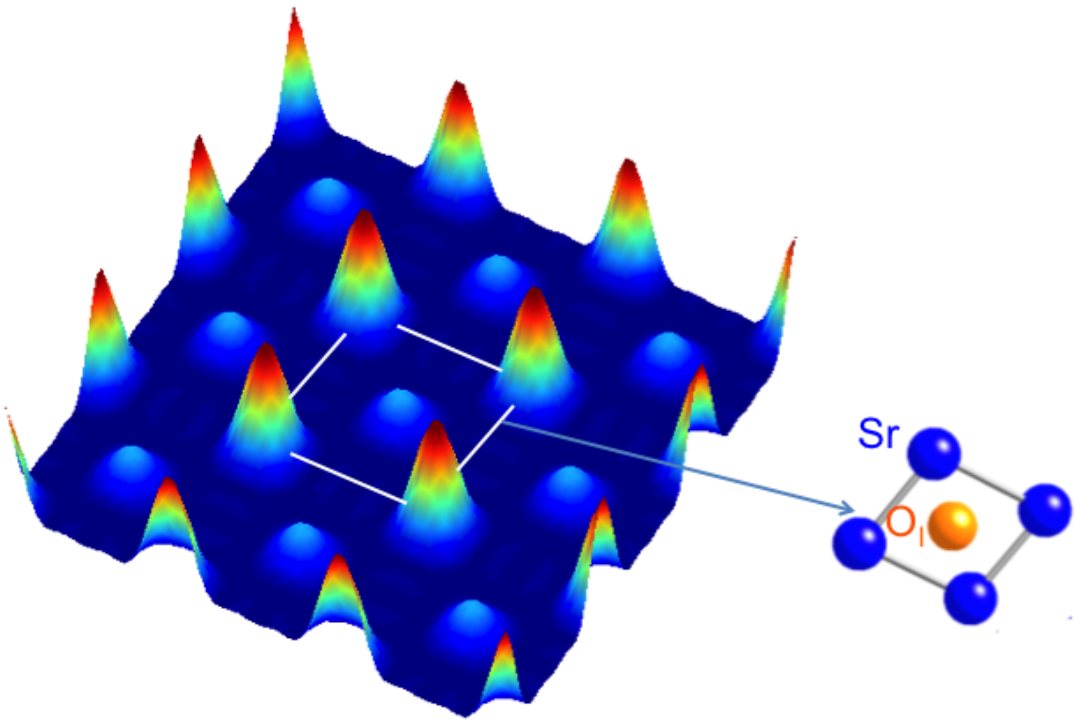

Figure S6. Plane cut of Sr-O_I layer in the substrate show visible Sr and O_I atoms.

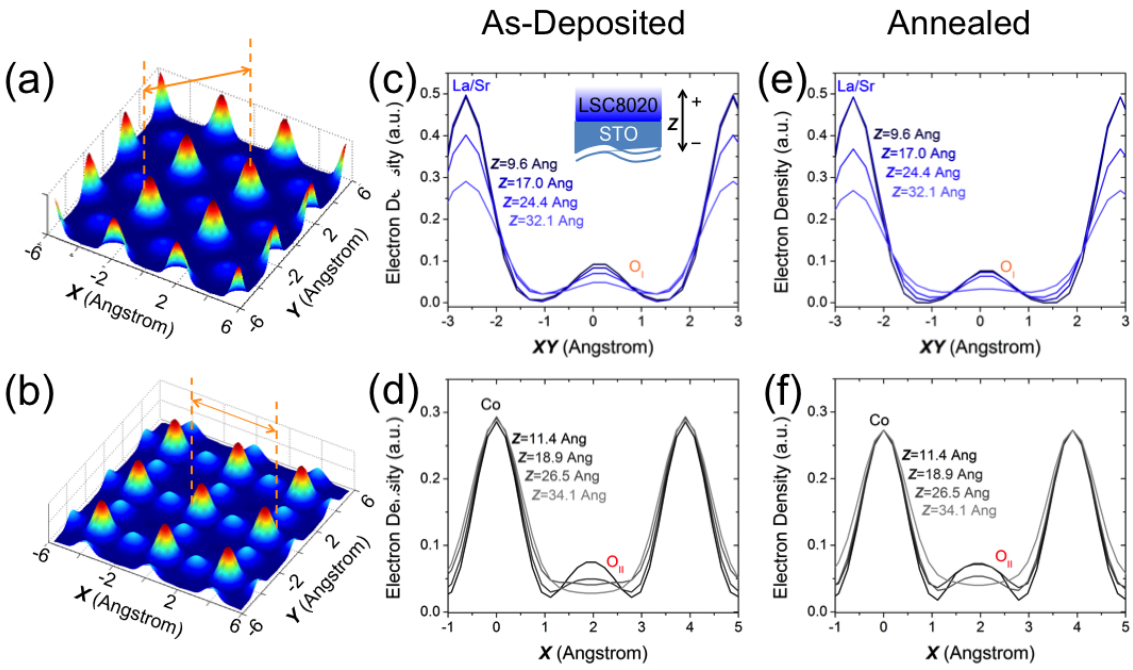

Figure S7. Electron density along lines on various planes parallel to the surface at different depths of LSCO/STO. Representative plane cuts of (a) La/Sr/O_I plane, and (b) Co/O_{II} planes. The orange line cuts are schematically shown in these planes. (c-d) lines for as-deposited, and (e-f) lines for annealed samples, for La/Sr/O_I and Co/O_{II} planes, respectively. A schematic inset in (c) shows the direction of the film surface. The O_I and O_{II} peaks decrease and broaden when approaching to the surface of the film, indicating the stronger disordering. Note equatorial O_{II} peaks decrease faster than apical O_I peaks.

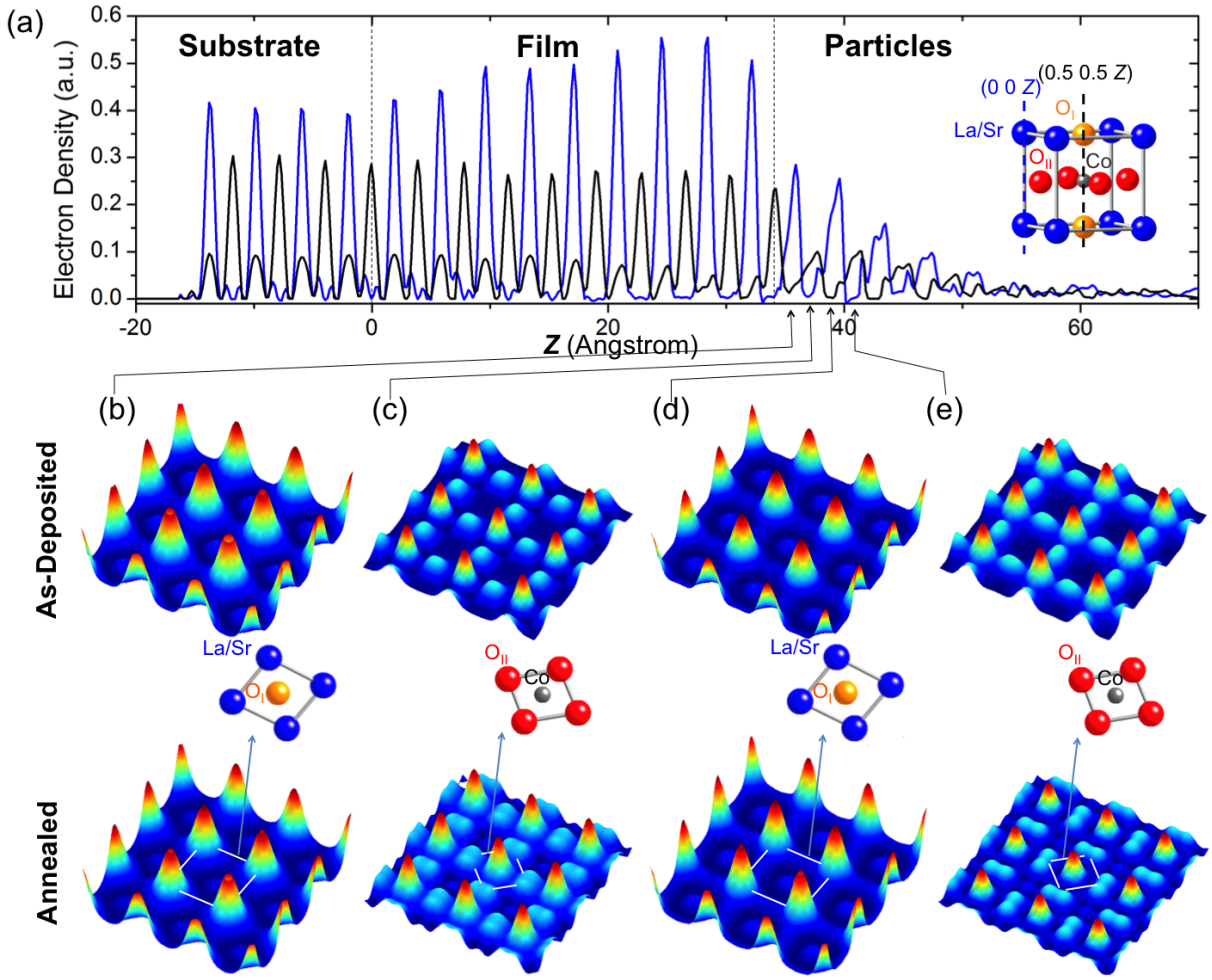

Figure S8. Electron density of the particle region on various planes parallel to the surface of $La_{0.8}Sr_{0.2}CoO_{3-\delta}$ (LSCO) on STO substrate. (a) The representative electron density of as-deposited LSCO/STO with a crystal model inset as the guide (blue and black are curves along the (0 0 Z) and (0.5 0.5 Z) lines, respectively). Black arrows indicate the positions of the in-plane cuts. (b) 1st bottom layer of the particles show La/Sr/O_I–like planes, (c) 2nd bottom layer of the particles show Co/O_{II}–like planes, (d) 3rd bottom layer of the particles show La/Sr/O_I–like planes, (e) 4th bottom layer of the particles show Co/O_{II}–like planes. The atomic structure of the particles show AO-BO2-AO-BO2 stacking, indicating the ABO_3 pervoskite structure.

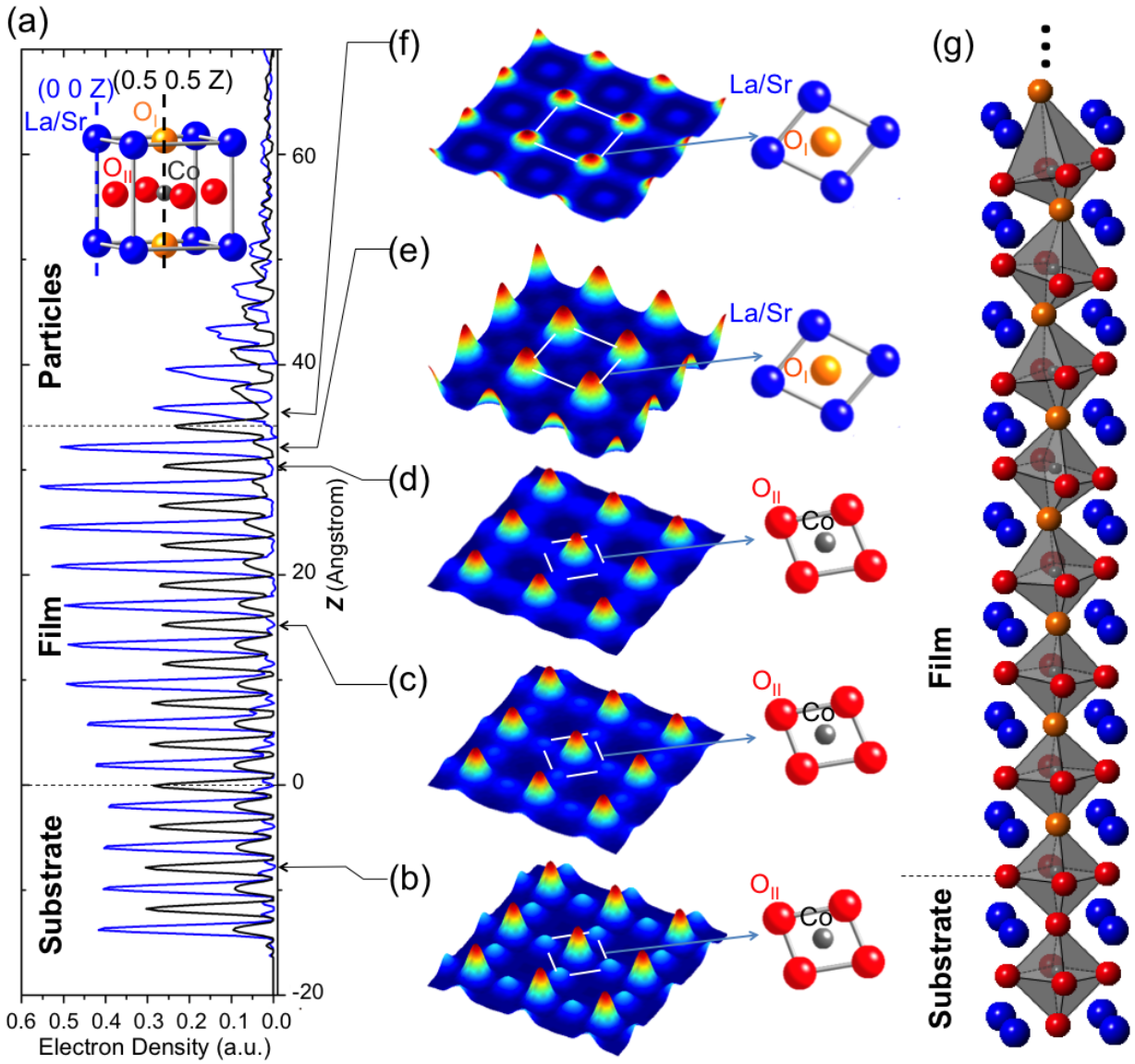

Figure S9. Electron density on various planes parallel to the surface of annealed $La_{0.8}Sr_{0.2}CoO_{3-\delta}$ (LSCO) on STO substrate. (a) The representative electron density of annealed LSCO/STO with a crystal model inset as the guide (blue and black are curves along the (0 0 Z) and (0.5 0.5 Z) lines, respectively). Black arrows indicate the positions of the in-plane cuts. (b) Substrate Ti/O_{II} plane, (c) LSCO "bulk" film $Co/Ti/O_{II}$ plane, (d) top of film $Co/Ti/O_{II}$ plane, (e) top of film $La/Sr/O_{I}$ plane, (f) island $La/Sr/O_{I}$ plane. (g) A crystal model of LSCO on STO substrate to illustrate the octahedral distortion observed from in-plane cuts. The octahedral distortion becomes stronger towards the film surface.

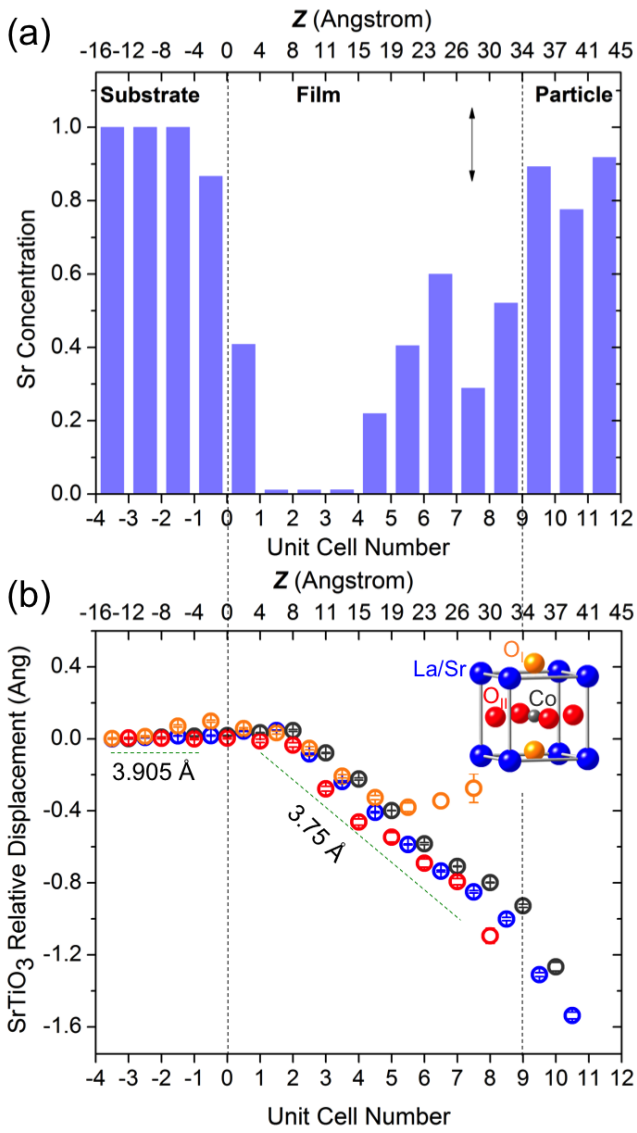

Figure S10. (a) Layer-by-layer Sr concentration vs. depth profile determined from differential COBRA method for LSCO annealed sample. The double arrow indicates the error bar. The black dashed lines represent the nominal substrate/film interface and film/particle interface, respectively. (b) COBRA-determined atomic positions of each type of atoms for annealed sample. The positions are shown as displacements relative to the corresponding atoms in an ideal STO lattice used as a frame of reference. The slopes of the dashed green lines indicate the lattice constants of those parts and a crystal model inset shows different types of atoms.

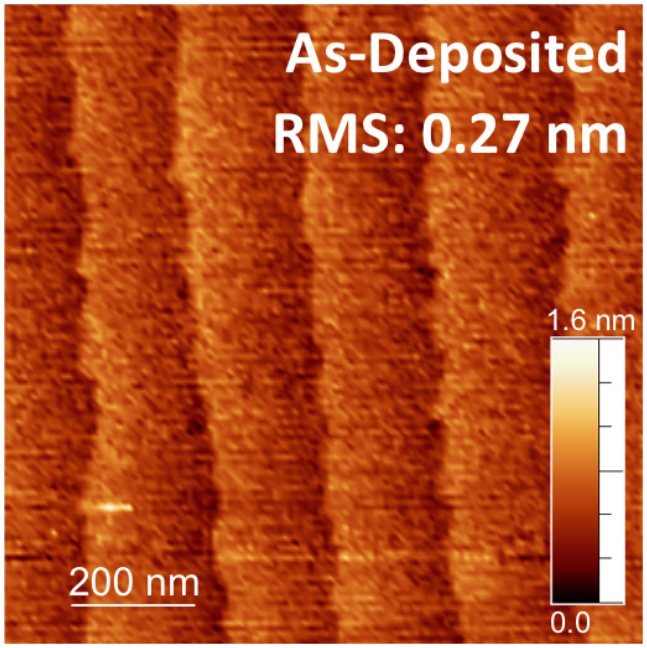

Figure S11. 1 × 1 μm^2 AFM image of as-deposited $La_{0.6}Sr_{0.4}CoO_{3-\delta}$ (LSCO6040) thin films grown epitaxially on $SrTiO_3$(001) substrate. These films were grown by PLD at ~550 °C under 200 mTorr partial oxygen pressure for 250 pulses, corresponding to 3 full unit cells or ~1.2 nm. The thickness was limited to achieve layer-by-layer growth and to avoid the creation of particles. Original terraces from STO substrate were still visible after the film deposition,

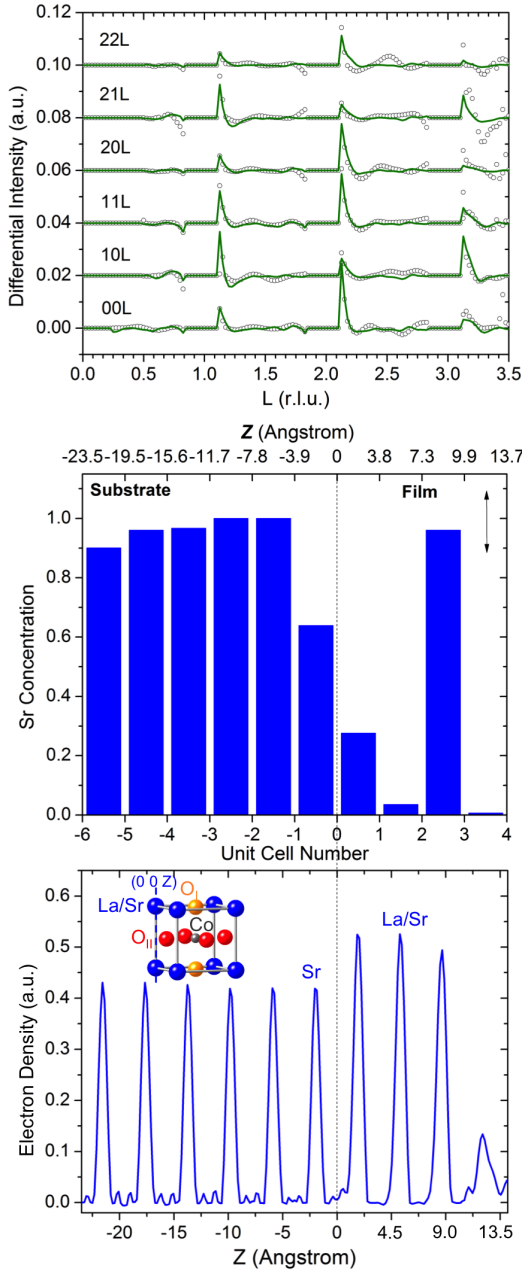

Figure S12. (a) Differential COBRA data (black circles) and fit (green lines) for 3 unit cells LSCO6040/$SrTiO_3$ (001) at as-deposited conditions. (b) Layer-by-layer Sr concentration vs. depth profile determined from differential COBRA method for LSCO6040. The double arrow indicates the error bar. The dashed black lines represent the nominal substrate/film interface. Strong Sr segregation is also found in the top unit cell. (c) The COBRA-determined electron density (EDY) along (0 0 Z) line shown in the crystal model insets of as-deposited LSCO6040 sample.

References

(1) Sowwan, M.; Yacoby, Y.; Pitney, J.; MacHarrie, R.; Hong, M.; Cross, J.; Walko, D. A.; Clarke, R.; Pindak, R.; Stern, E. A. *Physical Review B* **2002**, *66*, 205311.

(2) Elser, V. *Acta Crystallogr A* **2003**, *59*, 201.

(3) Zhou, H.; Pindak, R.; Clarke, R.; Steinberg, D. M.; Yacoby, Y. *J Phys D Appl Phys* **2012**, *45*, 195302.

(4) Yacoby, Y.; Zhou, H.; Pindak, R.; Bozovic, I. *Physical Review B* **2013**, *87*, 014108.

(5) Kumah, D. P.; Shusterman, S.; Paltiel, Y.; Yacoby, Y.; Clarke, R. *Nature Nanotechnology* **2009**, *4*, 835.

(6) Vailionis, A.; Boschker, H.; Siemons, W.; Houwman, E. P.; Blank, D. H. A.; Rijnders, G.; Koster, G. *Physical Review B* **2011**, *83*, 064101.

(7) Glazer, A. M. *Acta Crystallographica B* **1972**, *28*, 3384.

(8) Sathe, V. G.; Pimpale, A. V.; Siruguri, V.; Paranjpe, S. K. *Journal of Physics-Condensed Matter* **1996**, *8*, 3889.